Mass fractal dimension from 2D microscopy images via an aggregation model with variable compactness

Giulia Ferri, Severine Humbert, Jean-Marc Schweitzer, Mathieu Digne, Veronique Lefebvre, Maxime Moreaud

Mass fractal dimension from 2D-microscopy images via an aggregation model with variable compactness

Giulia Ferri[1,*], Severine Humbert[1], Jean-Marc Schweitzer[1], Mathieu Digne[1], Veronique Lefebvre[1] and Maxime Moreaud[1,2]

[1] IFP Energies Nouvelles, Solaize, Rhône, 69360, France
[2] CMM MINES ParisTech, PSL-Research University, Fontainebleau, Seine-et-Marne, 77305, France
[*] *present address: LCCP - Dipartimento di Energia, Politecnico di Milano via La Masa 34, 20156 Milano, Italy*

Microscopy-image analysis provides precious information on size and structure of colloidal aggregates and agglomerates. The structure of colloids is often characterized using the mass fractal dimension d_f, which is different from the two-dimensional fractal dimension d_p that can be computed from microscopy-images. In this work we propose to use a recent morphological aggregation model to find a relationship between 2D image fractal dimension and 3D mass fractal dimension of aggregates and agglomerates. Our case study is represented by scanning transmission electron microscopy-images of boehmite colloidal suspensions. The behaviour of the computed d_f at different acid and base concentration shows a fair agreement with the results of Small Angle X-Ray Scattering and with the literature, enabling to use the d_f vs d_p relationship to study the impact of the composition of the colloidal suspension on the density of colloidal aggregates and agglomerates.

keywords: fractal dimension, morphological model, image analysis.

1 Introduction

Image-analysis is frequently used to characterize colloidal particles of silica[1], alumina[2], soot or carbon. These particles can exist as a powder or within liquid suspensions, and they find applications in different domains like electronics, pharmaceutic and catalysis[3]. Such applications depend on particles size and structure that are the result of the particles aggregation or agglomeration mechanism[4;5;6]. For this reason the control of aggregation and agglomeration within colloids is of high importance. In literature, the terms aggregate and agglomerate are often used interchangeably. When it is necessary to distinguish between them, authors refer to the type of cohesive force that can be either strong or weak[7]. With regard to the colloidal boehmite suspensions characterised in this work, assemblies of maximum diameter lower than or higher than 80 nm are called aggregates or agglomerates, respectively.

The mass fractal dimension d_f is often used to characterize the structure of aggregates and agglomerates. Assuming that an aggregate/agglomerate consists of N identical spheres of radius a, the fractal dimension relates N to the gyration radius R_{gyr}[8;9;10].

$$N = k_f \left(\frac{R_{gyr}}{a} \right)^{d_f} \tag{1}$$

where k_f is the fractal pre-factor whose value varies typically between 1 and 1.2, depending on the fractal dimension itself[11]. The mass fractal dimension is close to unity for linear clusters and

increases up to a maximum value of 3 for clusters with several folded branches. d_f can be measured by experimental scattering techniques such as Small Angle X-Ray [12] or Neutron [13] Scattering. A change in d_f of a colloidal aggregate/agglomerate modifies its density, involving different dispersibility and settling behaviour [14]. This changes the workability of a colloidal suspension, as well as the textural properties of the solid obtained after a precipitation or drying process. In the context of γ-alumina catalyst carriers synthesis, the porosity of the final solid depends on the size and shape of the aggregates (meso-porosity $\simeq$ 10 nm) and agglomerates (macro-porosity $\simeq$ 100 nm) resulting from colloidal inter-particle interactions during different stages of preparation. By varying the chemical parameters of the colloidal suspension, it is possible to change the aggregation and agglomeration processes [15], leading to different size distribution and fractal dimension. Our interest is to use microscopy-image analysis to study this behaviour, in order to determine the physical-chemical parameters that lead to specific structure change within boehmite suspensions.

In this work, a characteristic fractal dimension d_p is computed from microscopy images of boehmite aggregates and agglomerates. d_p is then related to the mass fractal dimension d_f. A similar purpose has been addressed many times in literature. The fractal dimension computed on two-dimensional images depends on the calculation method used [16;17]. For this reason, in order to compare several images it is necessary to use the same computation algorithm. Other studies on the relationship between cluster mass fractal dimension and their projection report that for $2 < d_f < 3$ the difference $d_f - d_p$ increases with d_f [18].

In this work the projected fractal dimension d_p is measured using the relationship between area and perimeter [19]. This method is extensively used [20;21], enabling to obtain directly a two-dimensional fractal dimension from the slope of the graph $\log(P^2)$ vs $\log(A)$, where P and A are respectively the perimeter and the area of the projections. The slope tends to 1 for circular objects and to 2 for linear objects. Since the fractal dimension of the projection d_p is different from the mass fractal dimension d_f, a relationship between these two parameters [22;23;24;25;26] is needed.

The aim of our work is to numerically provide such relationship, using a recent morphological aggregation model [27]. The model is used to build clusters with a statistical average fractal dimension, as well as their opaque projections.

2 Determination of 3D-fractal dimension from 2D-microscopy images

In this section, we consider Scanning transmission electron microscopy (STEM) images of colloids of a boehmite suspension (on the left in Fig.1) and we explain the step-by-step strategy to extract d_f from such images.

2.1 Image processing and determination of d_p

To compute the perimeter and area on STEM images, several operations are applied. The image noise is reduced [28;29] by preserving the sharp edges of objects. Morphological black TopHat operator [30] is applied consisting on difference between the image and a morphological opening γ of the image, and a threshold operator tr_s such that

$$tr_s(I(x)) = \begin{cases} 1 | I(x) > s \\ 0 | I(x) \le s \end{cases} .$$

Extracted solid suspension can be expressed for an image I as $tr_s(I - \gamma_B(I))$ where s is obtained by inter-class variance maximization on the histogram of I [31], and B is the structuring element which
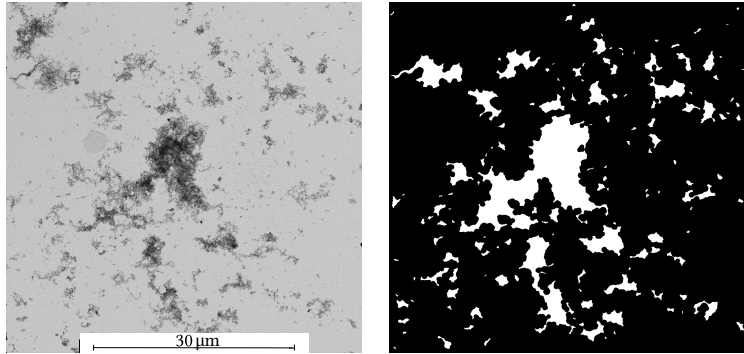
Figure 1: Experimental image (on the left) and its binary version (on the right).

in our case is a disc of radius 30 pixels. In order to reduce the remaining noise, the morphological operations of opening γ and closing φ are applied, defined for the image I and the structuring element C as $\gamma_C(I) = \delta_C(\varepsilon_C(I))$ and as $\varphi_C(I) = \varepsilon_C(\delta_C(I))$ where δ and ε are respectively morphological dilation and erosion[30], C is a disc of diameter 6 pixels. The last step of image cleaning consists in a hole filling and in the removal of the objects touching the edges of the image[30]. The holes are not always related to the existence of a real hole but rather to variations in thickness. While objects touching the borders would provide a misleading perimeter and area. Fig.1 reports an example of an experimental image and of the final binary image. On the binary images it is possible to calculate the perimeter P and area A of each object. The d_p is estimated from the slope of the line interpolating the experimental points on the plot $\log(P^2)$ vs $\log(A)$[19]. To estimate the d_f corresponding to a given d_p it is necessary to pass through a morphological model.

It is worth considering that the structures observed via STEM images are affected by the sample preparation process (drying under IR lamp). Furthermore, the choice of structuring element B can have a significant impact on the calculation of d_p. For this reason, in order to compare the results, it is important to prepare all samples following the same procedure and to perform the image analysis using the morphological operations in the same order and with the same structuring elements.

2.2 Morphological aggregation model

The morphological aggregation model[27] builds clusters consisting of N non-overlapping elementary objects arranged according to a given statistical average fractal dimension d_f. Clusters are built by sequential addition, assigning a different sticking probability to the points on the cluster. In particular, "concave points", leading to compact clusters, are distinguished from "non-concave" points, leading to loose structures. In addition the concave points closest to the center of mass of the cluster are distinguished as well, in these points the maximum compactness is reached. The model enables to obtain clusters with a fractal dimension d_f between 1.3 and 3. A fast scheme is available in case of spheres[27] and is used in this present work. A new object P is stuck to a cluster C either in a point on the cluster dilation

$$X_P = F(\delta_P(C)), \qquad (2)$$

3

either on a concave point of the dilation

$$X_P^{CV} = F\left(\delta_P(C)\right) \cap F\left(\varphi_r(\delta_P(C))/\delta_P(C)\right) \tag{3}$$

or in the concave point closest to the center of mass of the cluster C

$$X_P^M = x \in X_P^{CV} | \inf d(x, M). \tag{4}$$

The expression $\varphi_r(\delta_P(C))/\delta_P(C)$ means the difference between the two sets. $F(X)$ is the set of points at the border of X, $F(X) = \{z : B_z \cap \check{X} \neq \emptyset\}$, with B unit ball, M is the center of mass of the cluster C and $d(x, M)$ is the euclidean distance between the position x of the concave point and M. Fig.2 illustrates how the morphological operations enable to select the concave regions of a cluster's boundary. An implementation of this model is available on the plugim! platform [32].
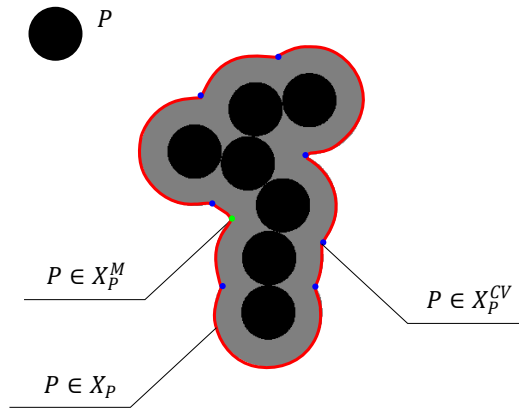

Figure 2: The dilated set X_P (in gray), the set of concave regions X_P^{CV} (in blue) and X_P^M are illustrated for a cluster C during the simulation. P is the primary particle.

2.3 Construction of d_f vs d_p chart

In order to compute d_p of a cluster generated by the model, it is necessary to generate the projections of numerous clusters for a given d_f in the largest range for N (the number of elementary spheres). The mass fractal dimension d_f of each cluster is determined with Eq.(1) using the plots reported in Appendix A. In the present study a fractal pre-factor k_f of 1.2 is used, in order to establish reference values for d_f of the clusters generated [27]. This value has been chosen because it provides a mass fractal dimension less than or equal to 3 for simulated clusters consisting of spherical particles.

The model inlet parameters were chosen in order to obtain a target statistical average $\overline{d_f}$. Only the clusters with $\left|d_f - \overline{d_f}\right| \leq 0.01$ were used to compute the projection. For each cluster, one orthogonal projection is computed, since a large number of simulations is performed it is possible to assume that area and perimeter computed on the projection are anisotropic. Fig.3 represents three-dimensional clusters with their projection for different number of elementary spheres N. A hole filling operation is performed to obtain projection comparable to experimental images [30]. The computation of area and perimeter enables the construction of the $\log(P^2)$ vs $\log(A)$ plot, whose slope is d_p [19].
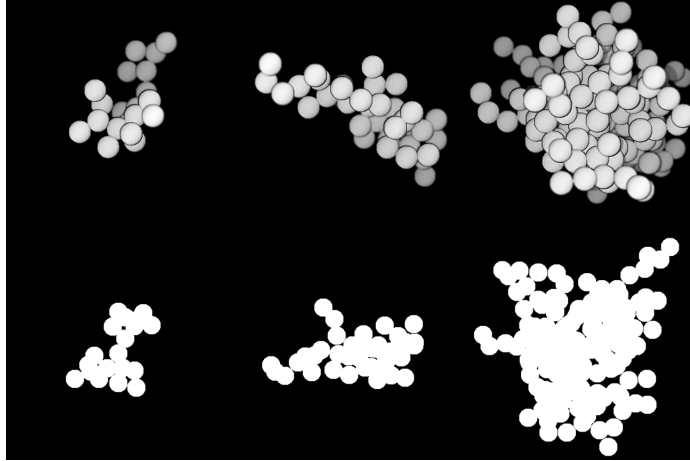
4

Figure 3: Illustration of three-dimensional clusters and their projections for $\alpha = \beta = 0.1$ and $N = 20, 40, 160$. α and β are the compactness parameters of the morphological aggregation model, more details are in Ferri et al.[27].

2.4 Relationship between d_p and and d_f

In Fig.4(a) the aggregation morphological model is used to compute the d_f vs d_p chart. The higher is d_f, the lower the d_p of its projection, similar results were obtained by Ehrl et al.[26], with a linear relationship between the two parameters. In our case a polynomial of third degree represents more accurately the results

$$d_f = 6.03 \cdot (d_p)^3 - 25.63 \cdot (d_p)^2 + 34.13 \cdot d_p - 11.55. \tag{5}$$

The coefficients of the polynomial minimize least-squares fit.

Eq.(5) is valid for the morphological aggregation model described in a previous work[27], using spherical primary particles. Since there is no one-to-one correspondence between the fractal dimension of a cluster d_f and the dimension of its projection d_p, it is not possible to conclude whether this relationship can also be valid for other random aggregation models.

2.5 Validity region

To compare experimental and model projections, the perimeter-area plots are represented as $\log(P^2)$ vs $\log(A/A_0)$, where A_0 is the projection of the elementary object forming the cluster.

Aggregation simulations were performed with a sphere of radius 10 pixels, corresponding to an opaque projection of area A_0 of 380 pixels. This is important so that the relationship shown in Fig.4(a) does not depend on the size scale and unit of measurement. The Eq.(5) is valid within limits, in terms of projected $\log(A/A_0)$, for a given d_f. The lower and the upper limit (respectively $l_{A,\min}$ and $l_{A,\max}$) are reported as reachable limit ranges by the aggregation model. The upper limit is also due to the maximum simulation volume, which in our case is of 10^9 voxels for time computing constraints.

The lower and the upper limits can be described as a function of d_f fitting respectively the lowest and the highest $\log(A/A_0)$ of the opaque projections of the simulated clusters.
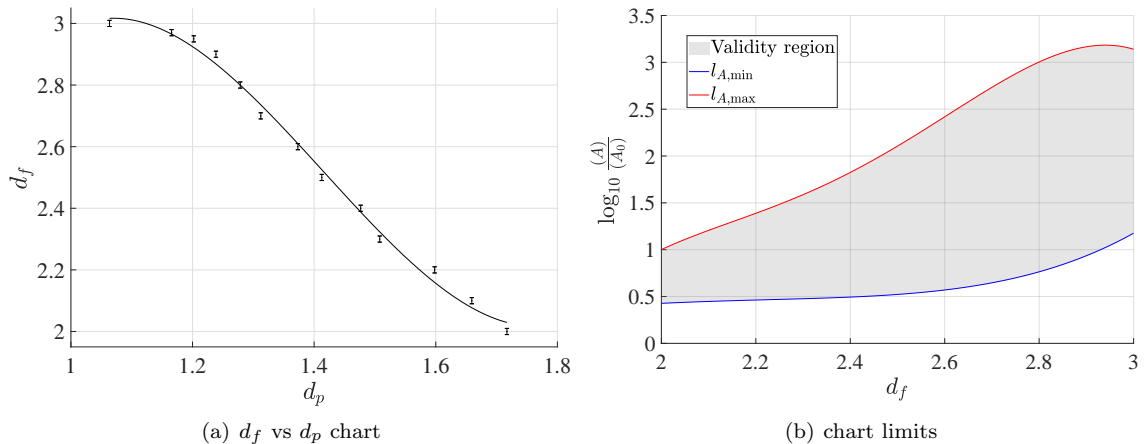
(a) d_f vs d_p chart

(b) chart limits

Figure 4: d_f vs d_p relationship described in Eq.(5) in (a) and its validity in terms of surface area A in (b).

$$
\begin{aligned}
l_{A,\min} &= 0.67 \cdot (d_f)^4 - 5.12 \cdot (d_f)^3 + 14.37 \cdot (d_f)^2 - 17.12 \cdot d_f + 7.49 \\
l_{A,\max} &= -7.17 \cdot (d_f)^4 + 68.19 \cdot (d_f)^3 - 241.09 \cdot (d_f)^2 + 377.70 \cdot d_f - 220.91.
\end{aligned}
\tag{6}
$$

The validity region and its limits are represented in Fig.4(b). A_0 does not influence the results for d_p, but only the domain of validity of the relationship in Eq.(5) on the $\log(P^2)$ vs. $\log(A/A_0)$ plot.

3 Experimental application to boehmite suspensions

In this section, we use the relationship between d_f and d_p to compute the mass fractal dimension from STEM images of different boehmite suspensions. Results are compared to Small Angle X-Ray Scattering and literature.

3.1 Boehmite suspensions preparation

Boehmite suspension are prepared with a highly dispersible powder from Sasol GmbH whose crystallites have the geometry of a rectangular beam with dimensions 5.2, 8.1 and 2.4 nm. These values are obtained from the X-Ray diffractogram using generalized Debye equation[2]. The colloidal suspensions are prepared with different concentration of 1M Fisher Scientific nitric acid (J/5550/PB15) and 1M Chem-Lab ammonia (CL05.0101.1000). The powder concentration is kept at 0.02 g/L in order to minimize overlapping in STEM images. The composition of the samples is shown in Tab.1. The table also reports the measured pH (Mettler-Toledo Seven2Go pH meter). A2 and B0 are the same suspension, which represents the initial conditions before ammonia addition (samples B1-3).

3.2 STEM Images Acquisition

A droplet of 10 µL of the suspension is deposited on copper grids with carbon membranes without holes and dried under IR lamp. After 2 min, the excess water is drawn off with a tissue paper.

6

Table 1: Composition, fractal dimension and average diameter of the boehmite suspension samples

Sample Name	HNO$_3$ [mM]	NH$_3$ [mM]	pH	d_p	d_f	D [nm]
A0	0	0	5.6	1.21	2.91	37
A1	0.75	0	3.4	1.26	2.83	22
A2-B0	1.5	0	2.9	1.28	2.79	21
A3	37.5	0	2.6	1.37	2.62	25
B1	1.5	1.9	4	1.37	2.62	682
B2	1.5	2.2	7.5	1.34	2.68	915
B3	1.5	3.2	9.6	1.22	2.90	1122

The samples are characterized with Scanning Transmission Electron Microscope (STEM), using a FEI Nova NanoSEM microscope operating at 15keV.

The different chemical parameters of the suspensions (acid and base concentration) of the samples causes the formation of structures ranging within a wide size range (10 nm - 10 µm). For this reason, the magnification level for a given sample is chosen in order to visualize the largest objects in their entirety. In particular we use a magnification of X 50000 for the samples A0, A1, A2 and A3, and a magnification of X 1500 is used for B1, B2 and B3.

3.3 Small Angle X-Ray Scattering

The analyses were performed at the SWING beamline at synchrotron SOLEIL in Saint Aubin, France. The boehmite suspensions are placed in a stirred reactor, from which the sample is pumped continuously through a quartz capillary of 1.5 mm, crossed by the X-ray beam, whose incident energy is 10 keV. The experiments are realized on an initial boehmite suspension analogous to the A2-B0 at 1 g/L. The SAXS curves measured 30 min after the base injection are fit with Beaucage model[33] in order to compute the mass fractal dimension. The model is detailed in Appendix B.

3.4 Monitoring of boehmite dispersion upon acid addition

The aggregates (observed in the samples A0, A1, A2 and A3) have an average diameter D between 20 and 40 nm (Tab.1). This diameter is calculated by averaging the diameters of objects on binary microscopy images. The diameter of each object is calculated as the average of the minimum and maximum diameters. For these objects A_0 is the one of an elementary crystallite. The average surface of the opaque projection of the crystallite is 38.25 nm^2, obtained by averaging on 1000 projections considering random 3D orientations[34] with a precision of 0.1 nm/voxels. Such estimation accounts for discretization issues, and it is close to the one computed using the Cauchy average projected area theorem, which is 37.02 nm^2.
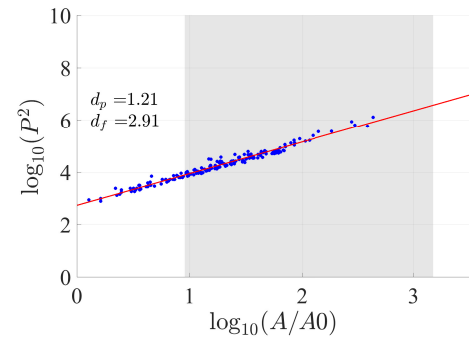We report the STEM images of the aggregates at different acid concentrations and their corresponding $\log(P^2)$ vs $\log(A)/\log(A_0)$ plots in Fig.5.

The grey regions in these graphs refer to the validity limits of the d_f - d_p relationship (Fig.4). The results of d_p and d_f (computed with Eq.(5)) are reported in Tab.1. The dispersion in acid leads to an increase in d_p, indicating the formation of loose structures. This is in agreement with d_f, and quite visible from the STEM images. The objects present in A3 are more elongated than the ones in A0-1. We observe a change of around 0.3 units of d_f. The difference between A3 and A2 is less noticeable, but the image processing enables to identify it. In conclusion, the acid content decreases fractal dimension of the boehmite suspension as it has been observed in other research works[35].
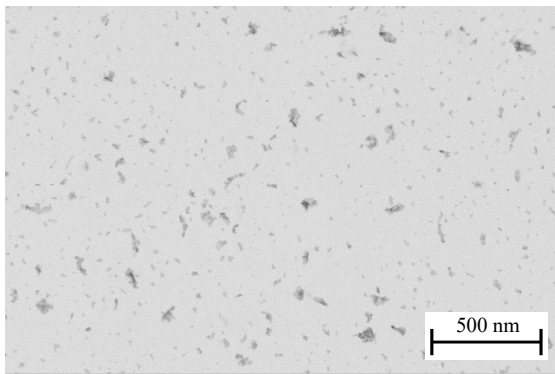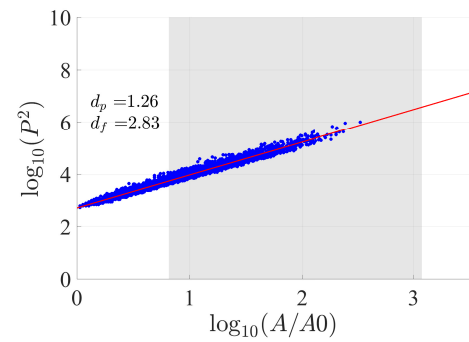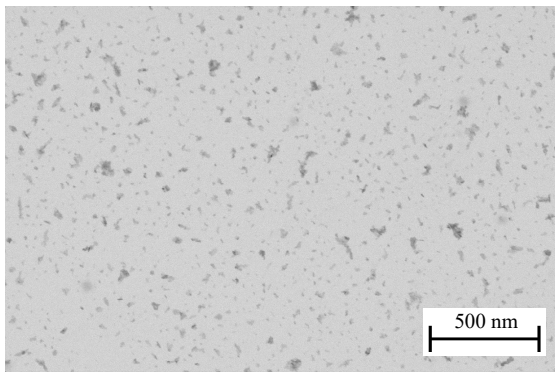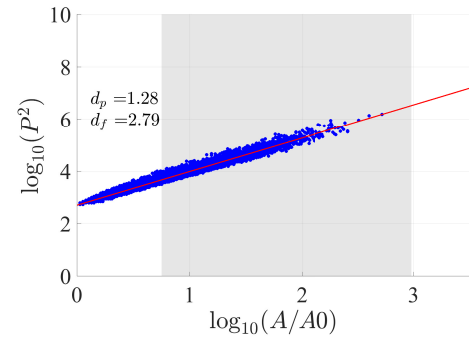
7
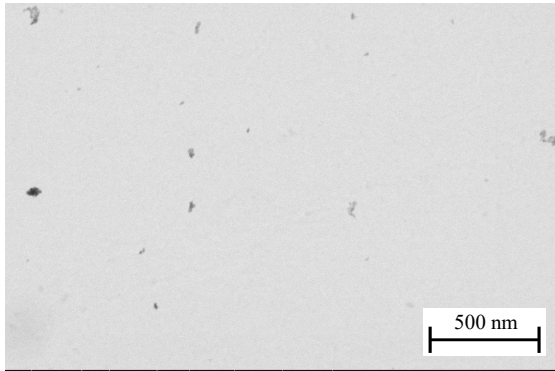
(a) STEM image of A0

(b) log(P) vs log(A) plot of A0

(c) STEM image of A1
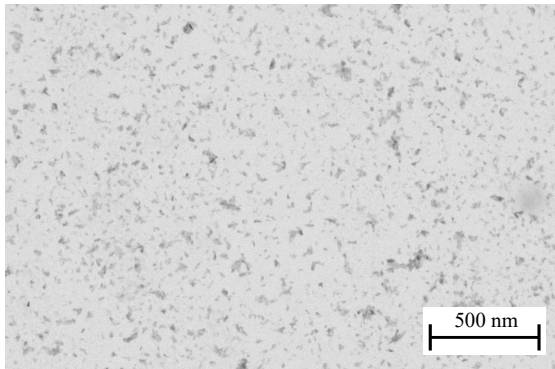
(d) log(P) vs log(A) plot of A1
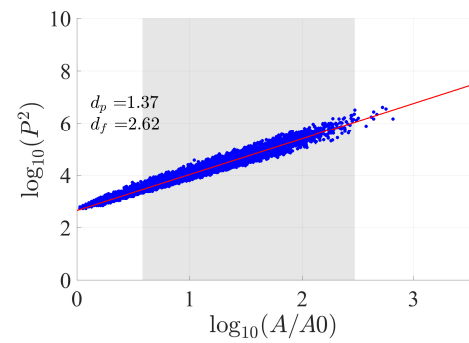
(e) STEM image of A2-B0

(f) log(P) vs log(A) plot of A2-B0

(g) STEM image of A3

(h) log(P) vs log(A) plot of A3

Figure 5: STEM images and $\log(P^2)$ vs $\log(A)$ plots of boehmite suspensions for varying acid content.

(a) STEM image of B1

(b) log(P) vs log(A) plot of B1

(c) STEM image of B2

(d) log(P) vs log(A) plot of B2
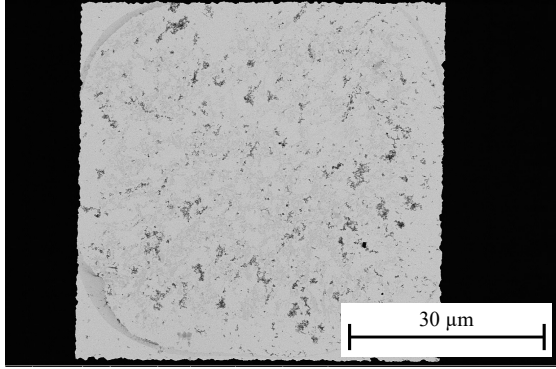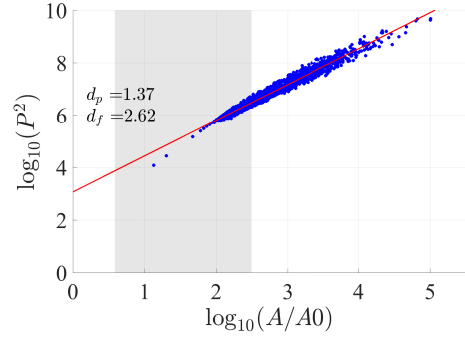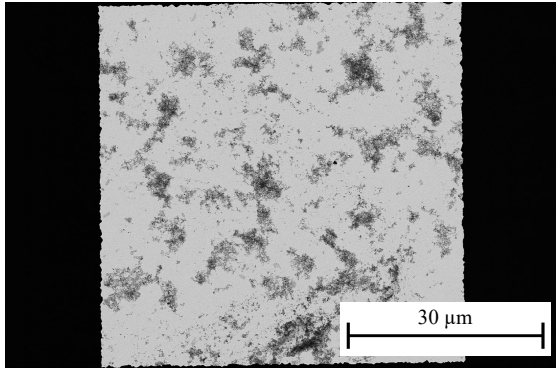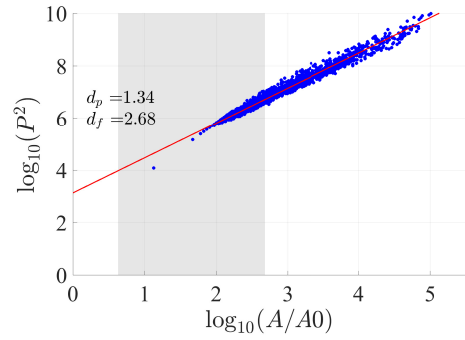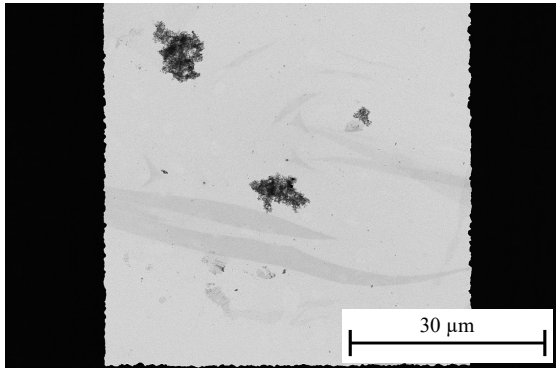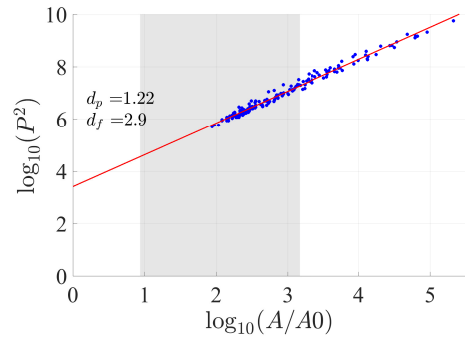
(e) STEM image of B3

(f) log(P) vs log(A) plot of B3

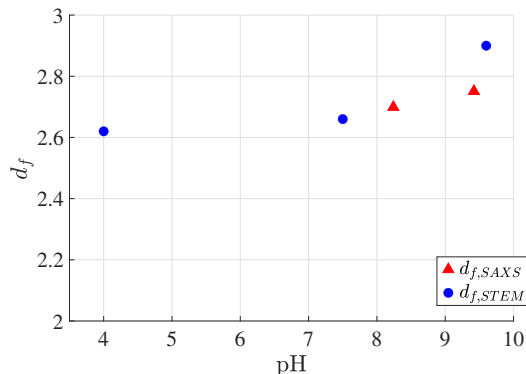Figure 6: STEM images and $\log(P^2)$ vs $\log(A)$ plots of boehmite suspensions for varying base content.

Figure 7: d_f computed via image analysis and Eq.(5), and measured with Small Angle X-Ray Scattering at different pH.

3.5 Monitoring of boehmite agglomeration upon alkaline addition

In a similar way, the relationship between d_f and d_p is used to characterize objects of a bigger scale, the agglomerates (in samples B1-3), obtained by ammonia addition to the suspension A2-B0. The average diameter D is of several hundreds of nanometers (Tab.1). In this case, the elementary particle is the aggregate, and A_0 was taken as the average area of the dispersed sample A2-B0, which is 453 nm^2. We now focus on the STEM images in Fig.6. The effect of the base content seems to favour the formation of more compact structures with a decrease in d_p. Between samples B1-2 and B3, we notice an evident change in the structure. Sample B3 presents highly compact objects Fig.6(e), for which the mass fractal dimension is 2.9. For B3 the pH is close to the Point of Zero Charge (PZC) of the suspension[36]. In these conditions the agglomeration is typically favoured[37]. We were able to observe an increase in the mass fractal dimension towards the PZC also with *in-situ* Small Angle X-Ray Scattering. Details on SAXS data are reported in Appendix B. The fractal dimension of SAXS agglomerates is compared to the one obtained from microscopy images in Fig.7.

The behaviour observed in SAXS results suggests that the proximity to PZC, besides favouring faster kinetics, leads to more compact structures. Since the operating conditions required by each analysis technique are different, a comparison can only be made on the basis of a trend. Even if the concentration and the sampling is different, the STEM image processing also showed that a pH close to PZC lead to more compact structures.

For a further improvement of our approach, it would be interesting to investigate in the future the effect of drying (under IR lamp) on the fractal dimension of boehmite agglomerates. Or to compare the fractal size estimated from scattering data with that obtained from liquid phase microscopy techniques.

4 Conclusion

The presented work provides a strategy to compute the mass fractal dimension from two-dimensional microscopy images. A relationship between d_p and d_f is numerically found using a recent morphological aggregation model. The mass fractal dimensions we obtained are in fair agreement with a visual estimate, enabling to use STEM images to determine the impact of different operating conditions on the structure of aggregates and agglomerated formed within a colloidal suspension. This

allows a better insight of the physical-chemical aspects that produce such structures In particular, we observed that an increase in acid concentration, causes the formation of more loose structures, with a decrease in d_f. While the increase of base content leads to more compact structures, leading to higher d_f. A complete validation of our approach is achieved by comparison of our results for boehmite suspension at different acid and base contents, with the literature and Small Angle X-Ray Scattering experiments.

Acknowledgment

Appendix

A   log(P) vs log(A) plots

This section shows the plots produced by relating the perimeter and area of the morphological model projections for $d_f = 2$, $d_f = 2.3$, $d_f = 2.5$ and $d_f = 3$ in Fig.8. The d_p is obtained from the slope of these plots.
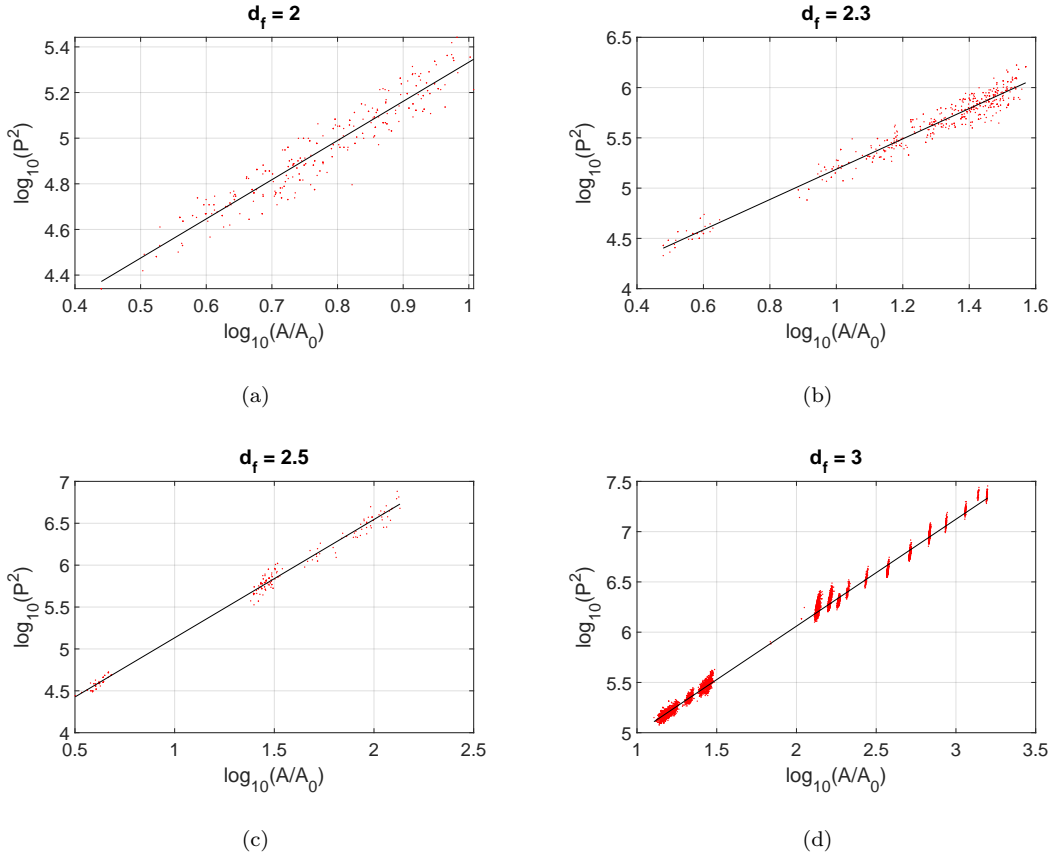

Figure 8: Log(P) vs log(A) plots obtained with the morphological model.

B SAXS data

B.1 Beaucage model

The general formula of the model for n structural levels is

$$I(q) = \sum_{i=1}^{n} G_i \cdot exp\left(- \frac{q^2 R_{gyr,i}^2}{3} \right) + B_i \left(- \frac{q^2 R_{gyr,i+1}^2}{3} \right) \cdot \left(\frac{\left(erf\left(q \cdot k_i \cdot \frac{R_{gyr,i}}{\sqrt{6}} \right) \right)^3}{q} \right)^{P_i} \quad (7)$$

- n equals to 1,2 or 3 for agglomerates, aggregates and crystallites respectively.

- G_i is the Guinier pre-factor depending on the number concentration of the structural unit $N_d \cdot r_e^2 \cdot \Delta\rho^2 \cdot V_i$ (N_d is the particles number density, r_e is the electron radius, $\Delta\rho$ is the electron density difference between the sample and the environment, V is the average particle volume).

- $R_{gyr,i}$ is the gyration radius.

- B_i is a constant pre-factor depending on the type of power-law scattering and on P_i [38].

$$B_i = \frac{G_i \cdot P_i}{R_{(gyr, i)}^{P_i}} \cdot \Gamma\left(\frac{P_i}{2} \right) \cdot \left(\frac{6 \cdot P_i^2}{(2 + P_i) \cdot (2 + P_i)} \right)^{\frac{P_i}{2}} . \quad (8)$$

- k_i is an empirical constant that depends on P_i [38], its value is close to 1.

- P_i is the slope of the curve in the structural level i, corresponding to the fractal dimension.

In our case, the SAXS curves present three scales. A nonlinear Least-Square Algorithm DN2FB [39] has been used for the curve fitting.

B.2 SAXS results

The scattering curve of a boehmite suspension at 1 g/L at pH close to the PZC (9.4) is reported in Fig.9. The three contributions of the simulated scattered intentity by agglomerates, aggregates and crystallites are illustrated.

The experimental data are fit within a range of 0.001255 $\mathring{A}^{-1}$ ¡ q ¡ 0.1998 $\mathring{A}^{-1}$ for the scattering vector. Corresponding to a maximum diameter ξ_l between 3 and 500 nm. According to the model, the agglomerates scatter in a range of 0.0078 $\mathring{A}^{-1}$ ¡ q ¡ 0.1998 $\mathring{A}^{-1}$, for a maximum diameter 80 nm ¡ ξ_l ¡ 500 nm according to the relationship

$$\xi_l = \frac{2\pi}{q}. \quad (9)$$

Due to the size limit of SAXS results, the comparison with microsopy images is made under the assumption that the fractal dimension is the same even for objects larger than 500 nm in diameter. This assumption can be confirmed in terms of d_p by the microscopy images analysis. Fig.10 shows a microscopy image of our boehmite suspension, its binary image and the relative plot $\log(P^2)$ vs $\log(A)$ in which the points relative to the objects with a maximum diameter higher and lower than 500 nm are highlighted in different colours. The points can be represented by the same line, and therefore by the same dimension d_p.
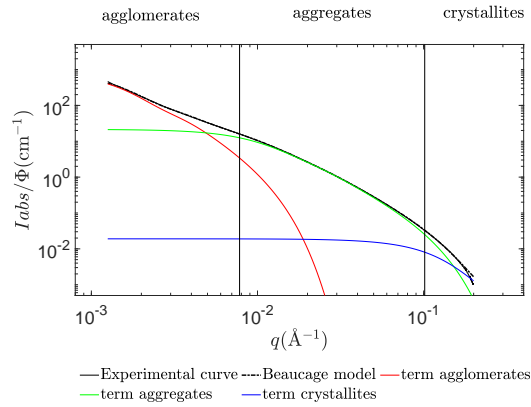
Figure 9: Experimental and simulated scattered intensity of a boehmite suspension at 1 g/L and pH close to the PZC. The simulated curve is given by the sum of three terms corresponding to agglomerates, aggregates and crystallites.
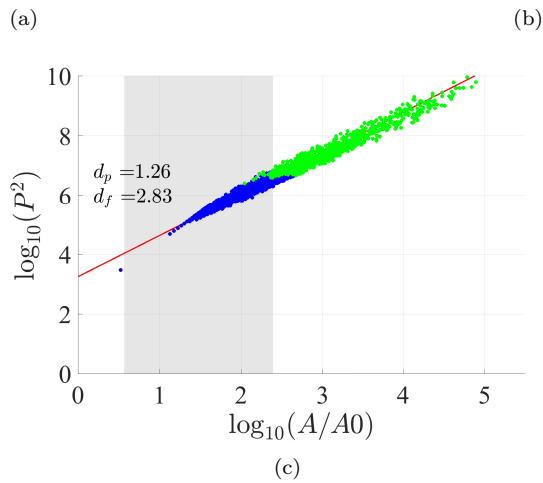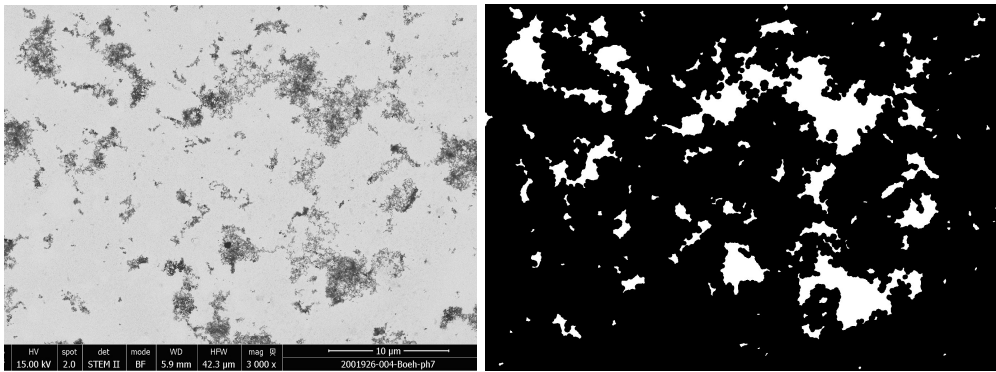
Figure 10: (a) STEM image of boehmite agglomerates obtained with a magnification of X 3000. Binary STEM image in (b). In (c) $log(P)$ vs $log(A)$ plot where the blue and green dots refer to the objects whose maximum diameter is below and above 500 nm respectively.

14

References

[1] Nelson Ibaseta and Béatrice Biscans. Fractal dimension of fumed silica: Comparison of light scattering and electron microscope methods. *Powder Technology*, 203(2):206–210, 2010. ISSN 00325910. doi: 10.1016/j.powtec.2010.05.010.

[2] David Chiche, Mathieu Digne, Renaud Revel, Corinne Chanéac, and Jean-Pierre Jolivet. Accurate determination of oxide nanoparticle size and shape based on X-ray powder pattern simulation: Application to boehmite AlOOH. *The Journal of Physical Chemistry C*, 112(23): 8524–8533, 2008. ISSN 1932-7447. doi: 10.1021/jp710664h.

[3] Harald Brune, Holger Ernst, Armin Grunwald, Werner Grünwald, Heiri Hofmann, Harald Krug, Peter Janich, Marcel Mayor, Wolfgang Rathgeber, Günter Schmid, Ulrich Simon, Viola Vogel, and Daniel Wyrwa. *Nanotechnology: Assessment and Perspectives*. Springer-Verlag Berlin Heidelberg, 2006. ISBN 978-3-540-32819-3. doi: 10.1007/3-540-32820-3.

[4] J. A. Witten and L. M. Sander. Diffusion-limited aggregation, a kinetic critical phenomenon. *Physical Review Letters*, 47(19):1400–1403, 1981. ISSN 0031-9007.

[5] P. Meakin. Formation of fractal clusters and networks by irreversible diffusion-limited aggregation. *Physical Review Letters*, 51(13):1119–1122, 1983. ISSN 0031-9007.

[6] D. A. Weitz, J. S. Huang, M. Y. Lin, and J. Sung. Limits of the fractal dimension for irreversible kinetic aggregation of gold colloids. *Physical review letters*, 54(13):1416–1419, 1985.

[7] Gary Nichols, Stephen Byard, Mark J. Bloxham, Joanne Botterill, Neil J. Dawson, Andrew Dennis, Valerie Diart, Niegel C. North, and John D. Sherwood. A review of the terms agglomerate and aggregate with a recommendation for nomenclature used in powder and particle characterization. *Journal of pharmaceutical science*, 91(10):2103–2109, 2002.

[8] Pramod Kulkarni, Paul A. Baron, Christopher M. Sorensen, and Martin Harper. *Nonspherical Particle Measurement: Shape Factor, Fractals, and Fibers*, chapter 23: 507–547. John Wiley & Sons, Ltd, 2011. ISBN 9781118001684. doi: https://doi.org/10.1002/9781118001684.ch23.

[9] Stephen R Forrest and Thomas A Witten Jr. Long-range correlations in smoke-particle aggregates. *Journal of Physics A: Mathematical and General*, 12(5):L109–L117, 1979.

[10] A V Filippov, Mauricio Zurita, and Daniel E Rosner. Fractal-like aggregates: Relation between morphology and physical properties. *Journal of Colloid and Interface Science*, 229(1):261–273, 2000. ISSN 0021-9797. doi: 10.1006/jcis.2000.7027.

[11] Christopher M Sorensen and Gregory C Roberts. The prefactor of fractal aggregates. *Journal of Colloid and Interface Science*, 186:447–452, 1997.

[12] Eugen Mircea Anitas. Small-angle scattering from fractals: Differentiating between various types of structures. *Symmetry*, 12(1):65, 2020. doi: 10.3390/sym12010065.

[13] Jose Teixeira. Small-angle scattering by fractal systems. *Journal of Applied Crystallography*, 21(6):781–785, 1988. ISSN 0021-8898. doi: 10.1107/S0021889888000263.

[14] Nelson Ibaseta and Beatrice Biscans. Ultrafine aerosol emission from the free fall of tio_2 and sio. 2007.

[15] Lawrence M Anovitz, Xin Zhang, Jennifer Soltis, Elias Nakouzi, Anthony J Krzysko, Jaehun Chun, Gregory K Schenter, T R Graham, Kevin M Rosso, James J De Yoreo, Andrew G Stack, Markus Bleuel, Cedric Gagnon, David F R Mildner, Jan Ilavsky, and Ivan Kuzmenko. Effects of ionic strength, salt, and pH on aggregation of boehmite nanocrystals: Tumbler small-angle neutron and x-ray scattering and imaging analysis. *Langmuir*, 34:15839–15853, 2018. doi: 10.1021/acs.langmuir.8b00865.

[16] Jean-F Soille, Pierre; Rivest. On the validity of fractal dimension measurements in image analysis. *Journal of visual communication and image representation*, 7(3):217–29, 1996.

[17] Jesus Angulo. Hölder exponents and fractal analysis on metric spaces using morphological operators. *hal-03108997*, 2021.

[18] M Tence, J. P. Chevalier, and Jullien R. On the measurement of the fractal dimension of aggregated particles by electron microscopy: experimental method, corrections and comparison with numerical models. *J. Physique*, 47:1989–1998, 1986.

[19] Benoit B Mandelbrot, Dann E Passoja, and Alvin J Paullay. Fractal character of fracture surfaces of metals. *Nature*, 308:721–722, 1984.

[20] Bingqiao Yang, Pengliang Huang, Shaoxian Song, Huihua Luo, and Yi Zhang. Hydrophobic agglomeration of apatite fines induced by sodium oleate in aqueous solutions. *Results in Physics*, 9:970–977, 2018. ISSN 22113797. doi: 10.1016/j.rinp.2018.03.049.

[21] Huijuan Xiu, Feiyan Ma, Jinbao Li, Xin Zhao, Lihua Liu, Pan Feng, Xue Yang, Xuefei Zhang, Evguenii Kozliak, and Yun Ji. Using fractal dimension and shape factors to characterize the microcrystalline cellulose (mcc) particle morphology and powder flowability. *Powder Technology*, 364:241–250, 2020. ISSN 00325910. doi: 10.1016/j.powtec.2020.01.045.

[22] Jenny A Nelson, Roy J Crookes, and S Simons. On obtaining the fractal dimension of a 3D cluster from its projection on a plane- application to smoke agglomerates. *Journal of Physics D: Applied physics*, 23(4):465–468, 1990.

[23] Ümit Ö Köylü, Gerard M Faeth, Tiago L Farias, and M Graça Carvalho. Fractal and projected structure properties of soot aggregates. *Combustion and Flame*, 100, 1995.

[24] C Oh and Christopher M. Sorensen. The effect of overlap between monomers on the determination of fractal cluster morphology. *Journal of Colloid and Interface Science*, 193(1997):17–25, 1997. ISSN 0021-9797.

[25] Augusto M Brasil, Tiago L Farias, and M Graça Carvalho. A recipe for image characterization of fractal-like aggregates. *Journal of Aerosol Science*, 30:1379–1389, 1999.

[26] Lyonel Ehrl, Miroslav Soos, and Marco Lattuada. Generation and geometrical analysis of dense clusters with variable fractal dimension. *The Journal of Physical Chemistry B*, 113(31):10587–10599, 2009. ISSN 1520-6106. doi: 10.1021/jp903557m.

[27] Giulia Ferri, Severine Humbert, Mathieu Digne, Jean-Marc Schweitzer, and Maxime Moreaud. Aggregation morphological model with variable compactness: application to colloidal system. *Image Analysis and Stereology*, 40(2):71–84, 2021.

[28] Michiyoshi Kuwahara, Kozaburo Hachimura, Eiho S, and Masato Kinoshita. *Processing of RI-Angiocardiographic Images*, pages 187–202. Springer US, Boston, MA, 1976. ISBN 978-1-4684-0769-3. doi: $10.1007/978-1-4684-0769-3_13$.

[29] Mark A Schulze and John A Pearce. A morphology-based filter structure for edge-enhancing smoothing. In *Proceedings of 1st International Conference on Image Processing*, pages 530–534, 1994.

[30] Serra Jean. Introduction to morphological filters. *Image analysis and mathematical morphology*, 2: 101–114, 1988.

[31] Nobuyuki Otsu. A threshold selection method from gray-level histograms. *IEEE Transactions on systems, man and cybernetics*, 9:62–66, 1979.

[32] "plugim!". an open access and customizable software for signal and image processing. *https://www.plugim.fr*.

[33] Gregory Beaucage and Dale W Schaefer. Structural studies of complex systems using small-angle scattering: a unified guinier/power-law approach. *Journal of Non-Crystalline Solids*, 172 –174: 797–805, 1994. ISSN 00223093.

[34] Maxime Moreaud, Dominique Jeulin, Vincent Morard, and Renaud Revel. Tem image analysis and modelling: application to boehmite nanoparticles. *Journal of Microscopy*, 245(2):186–99, 2012.

[35] Lucie Speyer, Séverine Humbert, Thomas Bizien, Vincent Lecocq, and Antoine Hugon. Peptization of boehmites with different peptization index: An electron microscopy and synchrotron small-angle x-ray scattering study. *Colloids and Surfaces A: Physicochemical and Engineering Aspects*, 603: 125175, 2020. ISSN 09277757. doi: 10.1016/j.colsurfa.2020.125175.

[36] Marek Kosmulski. ph-dependent surface charging and points of zero charge. iv. update and new approach. *Journal of Colloid and Interface Science*, 337(2):439–448, 2009. ISSN 0021-9797. doi: 10.1016/j.jcis.2009.04.072.

[37] Evert Johannes Willelm Verwey and Jan Theodoor Gerard Overbeek. *Theory of the stability of lyophobic colloids: the interaction of sol particles having an electric double layer*. Elsevier publishing company Inc., 1948.

[38] Boualem Hammouda. Analysis of the beaucage model. 2010.

[39] J.E Dennis, D. M. Gay, and R. E. Welsh. An adaptative nonlinear least-squares algorithm. *ACM Trans. Math. Softw.*, 7:348–368, 1981.